Supporting Information

Sustainable Lithium Recovery from Hypersaline Salt-lakes by Selective Electrodialysis: Transport and Thermodynamics

Zi Hao Foo,[†,‡] John B. Thomas,[†] Samuel M. Heath,[†] Jason A. Garcia,[¶] and John H. Lienhard[*,†]

†*Department of Mechanical Engineering, Massachusetts Institute of Technology, Cambridge, Massachusetts 02139, United States*

‡*Center for Computational Science and Engineering, Massachusetts Institute of Technology, Cambridge, Massachusetts 02139, United States*

¶*Department of Chemical Engineering, Massachusetts Institute of Technology, Cambridge, Massachusetts 02139, United States*

E-mail: lienhard@mit.edu

Number of Pages: 43. Number of Figures: 13. Number of Tables: 40.

Contents

List of Figures

List of Tables

A Computational Methods

A.1 Nernst-Planck Model for Ion Transport in Electrodialysis

Based on chemical thermodynamics, the fundamental relationship between the Gibbs free energy and the temperature, pressure and species mole fractions can be expressed as Eq. 1

$$dG = -SdT + vdP + \sum_i (RT \ln \gamma_i c_i + z_i F \Psi) dN_i \tag{1}$$

where S (J mol^{-1}) and T (K) denote the system entropy and temperature, v (m^3 mol^{-1}) and P (Pa) denote the specific molar volume and system pressure, and γ_i (-) and C_i (mol L^{-1}) denote the rational activity coefficient and concentration of species i, z_i (-), F (C mol^{-1}), Ψ (V) and N_i (mol) denote the ion valency, Faraday's constant, electric potential and molar quantity of species i, respectively.

Based on classical irreversible thermodynamics, the species molar flux can be modeled with the first spatial derivative of the species chemical potential, when the operating point is sufficiently close to thermodynamic equilibrium.[3] The Nernst-Planck (NP) equation, as described by Eq. 3, is obtained in combination with Eq. 1, in the isothermal and isobaric (NPT) ensemble

$$J_i = -L_i \frac{d\mu_i}{dz} \tag{2}$$

$$= -D_i^{mem} \nabla c_i^{mem} - \frac{D_i^{mem} z_i F}{RT} c_i^{mem} \nabla \Psi \tag{3}$$

where L_i denotes the proportionality constant in the chemical potential gradient and $D_i^{mem} = L_i RT / c_i^{mem}$ (m^2 s^{-1}) denotes the Fickian diffusion coefficient of species i. The terms in the NP equation correspond to ion transport from diffusion and electromigration, which are driven by the concentration and electric potential gradients, respectively.

For a binary salt, the expressions for the cation and anion fluxes can be written based on Eq. 3, as provided in Eq. 4 and 5

$$J_c = -D_c^{mem} \nabla c_c^{mem} - \frac{D_c^{mem} z_c F}{RT} c_c^{mem} \nabla \Psi \tag{4}$$

$$J_a = -D_a^{mem} \nabla c_a^{mem} - \frac{D_a^{mem} z_a F}{RT} c_a^{mem} \nabla \Psi \tag{5}$$

where subscripts c and a denote the cation and anion thermodynamic states and transport properties, respectively. Under the assumption of solution electroneutrality, the cation and anion fluxes are constrained by Eq. 6

$$J_a = \frac{I_{den}}{z_a F} - \frac{z_c}{z_a} J_c \tag{6}$$

where I_{den} (A m^{-2}) denotes the applied current density. The stoichiometry coefficients of the dissociated ions (ν_c and ν_a) can be related to their respective ionic valencies with Eq. 7. Further, the stoichiometry and diffusion coefficients of the dissociated ions can be related to the apparent salt diffusion coefficient with the Nernst-Hartley equation, as depicted in Eq. 8.

$$\frac{z_a}{z_c} = -\frac{\nu_c}{\nu_a} \tag{7}$$

$$D_{c-a} = \frac{(\nu_a + \nu_c) D_a D_c}{\nu_a D_c + \nu_c D_a} \tag{8}$$

The transport number of ion i, as represented by τ_i (-), which is defined as the fraction of the current conducted by the ion across the ion exchange membrane relative to the total applied current, can be expressed as a function of the ion concentration, diffusion coefficient and valency in Eq. 9.

$$\tau_i = \frac{z_i^2 D_i c_i^{mem}}{\sum_j z_j^2 D_j c_j^{mem}} \tag{9}$$

Together with classical solution-diffusion theory,[4] Eq. 4–9 can be condensed to obtain an explicit relationship between the cation and anion fluxes and the applied current density and concentration gradients, as provided in Eq. 10

$$J_i = \left\{ \frac{\tau_i I_{den}}{z_i F} + B_i \left[C_i^{d,int} - C_i^{c,int} \right] \right\} \tag{10}$$

where B_i (m s^{-1}) denote the solute permeability coefficient for diffusion, and $C_i^{d,int}$ (mol L^{-1}) and $C_i^{c,int}$ (mol L^{-1}) denote the solute concentration in the solution phase along the membrane-solution interface for the diluate and concentrate electrolyte streams, respectively. The model was

successfully generalized for multi-ionic mixtures by modeling the solutes as individual ions instead of binary salts.[5] As discussed in a prior publication from our group,[5] the transport number and solute permeability coefficient will become ion-specific, and are a function of the membrane properties and the feed composition, salinity and acidity. Experiments with multi-ionic solutions with the representative compositions must be used to accurately determine the respective coefficients.

The conventional Nernst-Planck equation assumes that the ion transport by convection is small as compared to the contributions from diffusion and electromigration.[5] This assumption typically holds for monovalent selective ion exchange membranes that are designed for salt production, as a result of their thick composite structure that renders the water permeability coefficients low.[1,6] To capture convective coupling between the solvent and ion transport in the event of significant transmembrane water flux, the model should be extended to include convection.[7] In this work, we experimented with multi-layered composite ion exchange membranes. Consequently, the IEMs are thick and the water permeability of the membranes is usually about an order of magnitude lower than unmodified IEMs.[6] With these membranes, our experiments indicated that the kinetics of water transport is approximately an order of magnitude lower the corresponding values for the ions, which aligns with recent reports.[2,6] As a consequence, the molar ion flux by convection (which is defined as the product of the ion concentration and the molar water flux[8]) accounts for less than 1 % of the total ion flux in all of our experiments. These results suggest that convection likely played a minor role in ion transport with the IEMs in this study.

Mass transfer limitations arising from concentration polarization in the electrolyte streams, as depicted in Fig. 2B, are incorporated with Eq. 11[9]

$$\Delta C_i = \left(\frac{\tau_i - t_{cu,i}}{D_i}\right)\left(\frac{I_{den}}{z_i F}\right)\left(\frac{2h}{\mathrm{Sh}}\right) \tag{11}$$

where ΔC_i (mol L^{-1}) denotes the concentration difference between the bulk flow and the membrane interface, $t_{cu,i}$ (-) is the integral counter-ion transport number of species i, D_i (m^2 s^{-1}) is the Fickian diffusion coefficient, h (m) is the channel height and Sh (-) is the Sherwood number. The Sherwood number is calculated based on mass transfer correlations proposed by McGovern et al.[9] for the spacers adopted in our experiments.

The integral counter-ion transport number, $t_{cu,i}$ (-), is calculated based on Eq. 12, in accordance

with the ED literature.[5,10] Following which, the limiting current density ($I_{den,i}^{lim}$) of the each ion is calculated to ensure that the experiments are conducted within the ohmic regime. Any current excess of this limit leads to water dissociation along the fluid-membrane interface, or accelerates the transport of multivalent and co-ions,[11] both of which negatively impacts the monovalent selectivity of the IEMs. The limiting current density for each ion i can be calculated with Eq. 13[5]

$$t_{cu,i} = \frac{z_i D_i C_i^{d,bulk}}{\sum_{j=1}^{N} z_j D_j C_j^{d,bulk}} \tag{12}$$

$$I_{den,i}^{lim} = \left(\frac{D_i z_i F}{\tau_i - t_{cu,i}}\right)\left(\frac{2h}{\mathrm{Sh}}\right) C_i^{d,bulk} \tag{13}$$

where h (m) denotes the characteristic length of the flow channels.

A.2 Counter-ion Transport across Ion Exchange Membranes

Ion exchange membranes (IEM) are water-swollen polymers that comprises two phases: 1) a charged gel phase formed by the hydrocarbon polymer chains and the hydrophilic ion exchange functional groups and 2) an interstitial phase formed from the pores, interstices and structural defects of the gel phase.[6] The void size is dictated by the swelling degree of the IEM, which is a function of the water volume fraction of the membrane.[2] In conventional ED literature, the interstitial phase is assumed to be filled by an electroneutral solution when the IEMs are contacted with a saline stream.[12]

Driven by an electrochemical potential gradient, ions partition from the solution to the interstitial phase of the IEM, and are transported across the IEM by diffusion and electromigration.[13] The ion selectivity of the IEM is governed by their respective ease of ion partitioning, and their respective mobilities within the interstitial phase. The Donnan exclusion mechanism is commonly employed to rationalize the relative differences in ion partitioning across the solution-membrane interface. Under this framework, the Gibbs free energy of the ions is assumed to be continuous across the solution-membrane interface to ensure chemical stability, as described in Eq. 14

$$\psi_i = \frac{\gamma_i^{mem} C_i^{mem}}{\gamma_i^{d,int} C_i^{d,int}} = f_w \left[\exp\left(-\frac{z_i F}{RT}\Delta\phi_{Donnan}\right)\right] \tag{14}$$

where f_w (-) represent the water volume fraction within the membrane, $\Delta\phi_{Donnan} = \phi_i^{mem} -$

$\phi_i^{d,int}$ (V) denote the Donnan potential and, γ_i^{mem} (-) and $\gamma_i^{d,int}$ (-) represent the ion activity coefficient within the membrane polymer and in the solution along the membrane-solution interface, respectively. The activity coefficients are predicted using Manning's counter-ion condensation[12,14] and Pitzer-Kim models,[15,16] using the method described by Fan and Yip.[2] Based on these theories, the ion concentration within the membrane phase is normalized by the volume of the interstitial phase of the IEM.[2,13]

Electroneutrality conditions are applied to the bulk solution and IEM's interstitial phases, as described by Eq. 15 and 16

$$\sum_i^N z_i C_i^{d.int} = 0 \tag{15}$$

$$C_{fixed}^{mem} + \sum_i^N z_i C_i^{mem} = 0 \tag{16}$$

where N (-) is the total number of ions and C_{fixed}^{mem} (mol L^{-1}) denotes the molar ion exchange capacity of the IEM.[17] Here, we set C_{fixed}^{mem} to be 1.68 M based on prior ion exchange capacity measurements on cation exchange membranes (CEM).[2,18] Eq. 14, 15 and 16 are solved simultaneously using the constrained trust region method to derive the concentrations of the partitioned ions and the resultant Donnan potential, implemented with numerical solvers in Python.[19]

The mobility of counter ions in polysulfonate CEM has received emerging interest in recent literature. Using an extended Mackie-Meares framework, Fan et al. demonstrated that a linear relationship exists between the ratio of the ion diffusion coefficient within the membrane relative to the bulk solution, and the exponential of the square of the ionic valency.[13] The observed reduction in the apparent diffusion coefficient within the polymer matrix arises from spatial hindrance from the tortuosity of interstitial phase, and the electrostatic friction between the cations and the ion exchange groups.[20] The relationship between the bulk and interstitial phase diffusion coefficients is given by Eq. 17.

$$D_i^{mem} = D_i^{d,int} \left(\frac{f_w}{2 - f_w} \right)^2 \exp(-A_{el} z_i^2) \tag{17}$$

where D_i^{mem} (m^2 s^{-1}) and $D_i^{d,int}$ (m^2 s^{-1}) denote the ion diffusion coefficient within the interstitial and bulk solution phases, respectively, and A_{el} (-) represents an electrostatic friction parameter that is a function of the fixed charge density (C_{fixed}^{mem}) and the apparent dielectric constant. A_{el}

is commonly employed as a regression parameter in IEM diffusion experiments, and the derived constant ranges between 0.329 to 0.691 for commercial CEMs.[13]

The Nernst-Planck equation is utilized in combination with the extended Mackie-Meares and Donnan equilibria models to analyze the implications of current density increments. Based on our experiments, when the applied current density is 2.5 mA cm^{-2} or higher, we found that ion transport by electromigration dominates; this conclusion is corroborated by prior experimental and computational studies.[10,21,22] When concentration-driven diffusion is small as compared to electric potential-driven electromigration, based on the Nernst-Planck equation, the ratio of ion fluxes between two distinct species tends towards the expression given by Eq. 18.

$$\frac{J_i^{Mod.}}{J_j^{Mod.}} \rightarrow \frac{D_i^{mem}}{D_j^{mem}} \frac{z_i}{z_j} \frac{C_i^{mem}}{c_j^{mem}} \tag{18}$$

Eq. 14 and 17 are leveraged to relate the ion concentration and diffusion within the interstitial phase to the bulk solution phase. The resultant expression is provided by Eq. 19

$$\frac{J_i^{Mod.}}{J_j^{Mod.}} = \frac{D_i^{d,int}}{D_j^{d,int}} \frac{z_i}{z_j} \frac{C_i^{d,int}}{C_j^{d,int}} \overline{\gamma}_{i,j} \exp\left[-A_{el}\left(z_i^2 - z_j^2\right)\right] \exp\left[-\frac{\Delta\phi_{Donnan} F}{RT}\left(z_i - z_j\right)\right] \tag{19}$$

where $\overline{\gamma}_{i,j}$ (-) represents the ratio of activity coefficients between the solution and the interstitial phase, between species i and j, respectively. For calculations of Li/Mg and Na/Mg flux ratios, the $\overline{\gamma}_{Li,Mg}$ and $\overline{\gamma}_{Na,Mg}$ ranges between 0.2874 – 0.2954 and 0.2698 – 0.2948, respectively. In this expression, the Donnan potential and the interfacial concentrations are functions of the applied current density, while A_{el} is a constant material parameter for a given CEM. The L^2-norm error between the experimental and model ion flux ratios is minimized using the constrained trust region algorithm. The derived A_{el} value is 0.412, which is within the reported range for commercial CEMs (0.329 - 0.691).

Eq. 19 indicates that the ion flux ratio between two species is proportional to the interfacial concentration ratio and two exponential terms. The first exponential term (defined as the mobility factor) corresponds to the differences in the ion mobility arising from electrostatic friction within the CEM[13] while the second exponential term (defined as the partitioning factor) corresponds to the differences in ion partitioning from Donnan exclusion.[6] Multivalent cations experience stronger

electrostatic friction within the CEM due to interactions with the negatively charged sulfonate moieties.[2,6] Therefore, the mobility factor between monovalent and multivalent cations is greater than unity. An increment in the applied current density leads to a reduction in the ion concentrations along the membrane-solution interface, improving the effectiveness of Donnan exclusion in rejecting multivalent ions. This leads to an increase in the resultant Donnan potential, amplifying the partitioning factor across the interface. When the applied current density is amplified, the combination of the mobility and partitioning factors in Eq. 19 induces a larger than proportional increase in the resultant ion flux ratios between monovalent and multivalent ions.

A.3 Impact on Ion Partitioning and Overall Selectivity

Ion selectivity is a result of differences in 1) ion partitioning and 2) ion mobility across the membrane.[6,23] In this study, a two-pronged computational approach was adopted to investigate the ion selectivity of the composite cation exchange membranes. In the first approach, as described in Section 2.3 and Section A.1 of the SI, the transport numbers of the respective ions under different operating conditions (i.e., current densities, feed salinities, composition and solution pH) were determined, and were systematically compiled in Supp. Table 40. As described in Eq. 1 and 2, the transport number is defined as the proportion of current conducted by the ion relative to the total applied current, and it characterizes the combined effects of ion partitioning and mobility for electromigration across the IEM.[5,23] As a result, the effective ion selectivity of both the PEI surface layer and the PS-DVB substrate is captured by the regressed transport numbers in our study. The separation factors were calculated with Eq. 1 and 2, leveraging the derived transport numbers and ion permeability coefficients.

In the second approach, as described in Section 2.3 and Section A.2 of the SI, we seek to understand the impact of the feed solution concentration and solution pH on efficacy of Donnan exclusion for multivalent cation rejection, using the method developed by Fan and Yip.[2] This approach was selected because prior studies on hypersaline electrodialysis indicated that the weakening of Donnan exclusion was the primary mechanism for the observed reduction in counter-ion/co-ion selectivity with high concentration feed solutions.[2,24] In accordance with the theory of Donnan exclusion, the ion concentrations within the PEI surface layer were simulated with Eq. 3,[2] and are presented

in Supp. Fig 13. Donnan exclusion from the positively-charged surface layer reduces the partitioning rate of multivalent cations, as a consequence of their higher charge densities.[25] Therefore, the monovalent ions (i.e., Li^+, Na^+, K^+) have a greater partition coefficient as compared to Mg^{2+}, aligning with the relative ion transport rates observed in Supp. Fig. 2 – 12. Given that the PS-DVB substrate is negatively charged, exclusion of cations by the Donnan effect is negligible across the interface between the PEI surface layer and the PS-DVB substrate.[25]

B Experimental Methods

B.1 Experimental Apparatus

The bench-scale experimental setup that is employed for membrane characterization is depicted in Supp. Fig. 1. The cathode and anode are fashioned from platinum-coated titanium electrodes. A total of 20 feed spacers and 2 end spacers, each with a 0.5 mm thickness and a 45 ° mesh orientation, are placed in the electrolyte channels. Sodium sulfate (0.2 M) solutions are used as the catholyte and anolyte to suppress chlorine gas production and stabilize the solution pH.[26] The diluate, concentrate and rinse circuits, comprising 2L, 4L and 4L of the respective solutions, are operated in a batch configuration. By starting with the same composition and concentrations on both streams, the contribution from concentration-driven diffusion can be decoupled and minimized between the experiments.[27] A larger concentrate solution volume is selected to slow the rate of increase of concentrate stream over the course of the experiment, reducing the impact of ion transport from back-diffusion.[1] Cross-flow is maintained at 95 L h^{-1} with centrifugal pumps (Iwaki MD55R) and valved rotameters. A potentiometric feedback loop regulates the temperature of the solutions and a DC power supply generates the electric potential gradient for ion transport (GW Instek GPR-60600). The solution volumes are monitored with digital mass scales (Ohaus Scout Pro SP601). The solution conductivity, pH, cell potential difference and temperature are recorded at 60 Hz with a digital acquisition unit (Vernier LabQuest, Hach HQ440d). The concentrate and diluate solutions are sampled periodically and analyzed with ICP-OES. The wavelengths of the respective elements are selected to avoid signal interference, and are summarized in Supp. Table 1.

The experiments in this study were all conducted at a constant current density to accurately

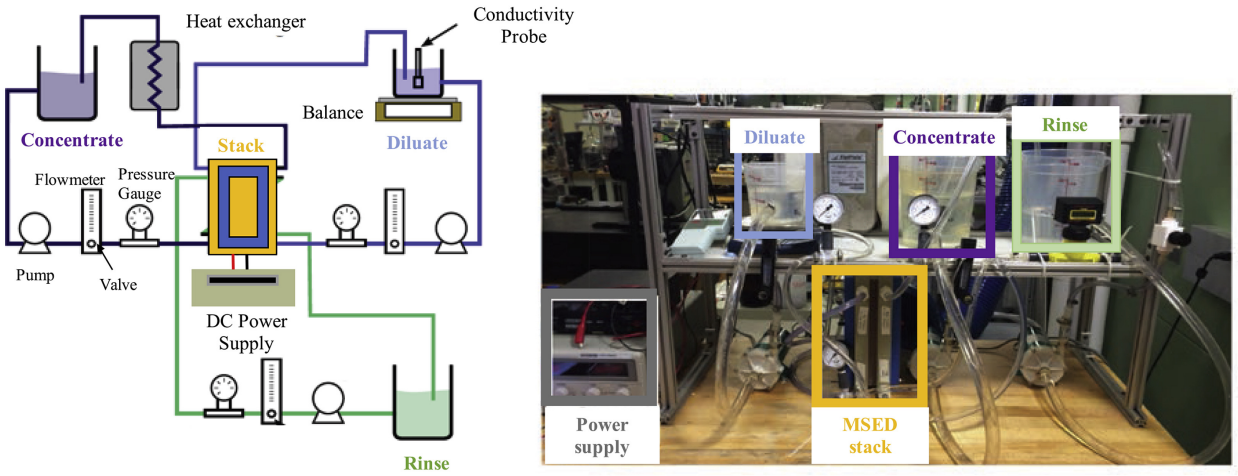

Supplementary Figure 1: Schematic diagram of the bench-scale electrodialysis adopted in this investigation. The diluate, concentrate and rinse loops are composed of 2, 4 and 4 L of electrolyte solutions, are cycled through the electrodialysis stack with centrifugal pumps. Over 10 alternating cell pairs of CEMs and AEMs comprise the membrane stack, which is housed inside of a PCCell ED 200 unit. A counter-flow heat exchanger regulates the electrolye stream temperatures to a pre-set value. An external direct current power supply is used to generate the potential difference for ion transport. The illustration is adapted from our prior publication and used with permission from Elsevier.[1]

characterize the transport numbers of the respective ions.[5,10] This is because the transport numbers are defined as the proportion of the current conducted by a particular species, and constant current conditions ensure that the normalization is standardized between the various experiments.[5,10] In our bench-scale setup with 10 cell pairs, the majority of the voltage drop occurs at the electrodes.[1] In the event of unprecedented side redox reactions, we would likely observe effervescence in the rinse loop or solid deposition at the electrodes.[10] However, we did not observe any noticeable changes between the different current densities during our experiments.

Supplementary Table 1: Selected wavelengths for spectroscopic analysis with ICP-OES.

Elements	ICP-OES wavelength (nm)
Na	568.263
K	404.721
Li	610.365
Mg	277.983
Cl	774.497
S	180.669

B.2 Solution Composition and Results

In this paper, experiments are conducted on binary cation and multicomponent salt-lake brines from Chile and China to ascertain the relative ion transport rates. The ionic composition of the solutions are provided in Supp. Tables 2, 3 and 4, respectively. The feed salinities vary from 10 to 250 g/L, the solution pH from 3 to 7, and the current density from 2.5 to 30.0 mA cm^{-2}.

The ion composition of the diluate stream is characterized based on ICP-OES. The propagated uncertainties in the respective ion concentration are all under 4.5 %. To provide a comprehensive database upon which future IEMs can be compared against, the experimental results are systemically tabulated. Using the computational framework described in Section A, the ion transport number, Donnan potential and the electrostatic friction parameter are determined based on Eq. 8 in the main text, for each of the tested compositions. The ion-specific permeability coefficients were determined based on diffusion experiments with multi-ionic feed solutions as described in our prior publications.[1,5,26] The agreement between the model predictions and the empirical measurements is illustrated in Supp. Fig. 2-12.

Ion selectivity arises as a result of differences in 1) ion partitioning and 2) ion mobility across the membrane.[5,6] The ion selectivity sequence for a variety of selective electrodialysis membranes has been systematically compiled in review articles by Luo et al.[6] and Ying et al.[28] In general, Donnan exclusion reduces the partitioning rate of multivalent ions, as a consequence of their higher charge densities.[2] Therefore, the monovalent ions (Li^+, Na^+, K^+) have a greater partition coefficient as compared to Mg^{2+}, aligning with the relative ion transport rates observed in Supp. Fig. 2 – 12. In accordance with the theory of Donnan exclusion, the ion concentrations within the PEI surface layer were simulated with Eq. 3 and are presented in Supp. Fig 13.[2] The model indicated that the relative concentrations of Li^+ to Mg^{2+} within the IEM increased up to 10, as compared to 1.8 in

Supplementary Table 2: Nominal ionic composition of binary cation feed solutions based on brine from Salar de Atacama, at a solution molarity of 0.35 M.

Brine Composition (Abbreviation)	**Nominal Composition (g/L)**					Solution Molarity (M)
	Li^+	Mg^{2+}	Cl^-	SO_4^{2-}	TDS	
Li^+-Mg^{2+}-Cl^- (LM-C)	0.34	2.05	7.70	0.00	10.09	0.35
Li^+-Mg^{2+}-SO_4^{2-} (LM-S)	0.49	2.98	0.00	15.13	18.59	0.35
Li^+-Mg^{2+}-Cl^--SO_4^{2-} (LM-CS)	0.34	2.09	7.39	0.62	10.44	0.35

Supplementary Table 3: Nominal ionic composition of feed solution based on brine from Salar de Atacama, Chile, at total dissolved concentrations of 10, 30, 70 and 250 g/L.

Salt Lake, Location	**Nominal Composition (g/L)**							
	Li^+	Na^+	K^+	Mg^{2+}	Ca^{2+}	Cl^-	SO_4^{2-}	TDS
Salar de Atacama, Chile	1.19	69.01	17.89	7.31	< 0.01	143.72	12.06	251.18
	0.33	19.23	4.99	2.04	< 0.01	40.10	3.36	70.00
	0.14	8.24	2.14	0.87	< 0.01	17.17	1.44	30.00
	0.05	2.75	0.71	0.29	< 0.01	5.72	0.48	10.00

Supplementary Table 4: Nominal ionic composition of feed solution based on brine from Qaidam Lake, China, at total dissolved concentrations of 10, 30, 70 and 250 g/L.

Salt Lake, Location	**Nominal Composition (g/L)**							
	Li^+	Na^+	K^+	Mg^{2+}	Ca^{2+}	Cl^-	SO_4^{2-}	TDS
Qaidam Lake, China	0.31	56.30	4.40	20.20	< 0.01	134.20	34.10	249.51
	0.09	15.79	1.23	5.67	< 0.01	37.65	9.57	70.00
	0.04	6.77	0.53	2.43	< 0.01	16.14	4.10	30.00
	0.01	2.26	0.18	0.81	< 0.01	5.38	1.37	10.00

the feed solution.

Due to the smaller differences in charge density between the monovalent ions, Donnan exclusion does not significantly influence the relative partitioning rate of Li^+ compared to Na^+ and K^+. Despite that, as illustrated in Supp. Fig. 2 - 12, our experiments reveal faster transport rates for Na^+ and K^+. The differences in relative transport rates of the monovalent cations have been rationalized in the literature by their respective mobilities within the ion exchange membrane.[6,13] The order of the diffusion coefficients follows the descending sequence: $H_3O^+ > K^+ > Na^+ > Li^+$, which agrees with our experiments, as illustrated in Supp. Fig. 2 – 12.

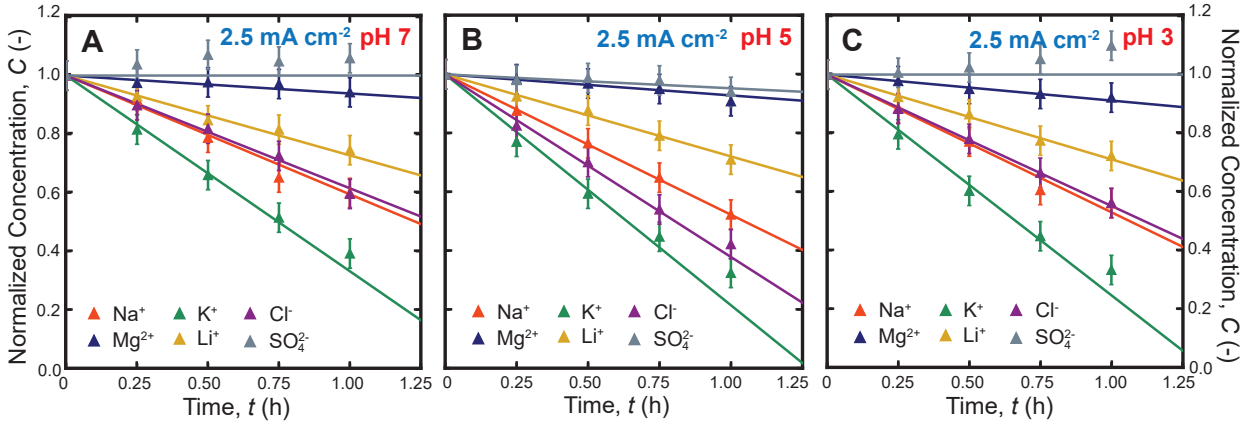

Supplementary Figure 2: Comparisons between the experimental measurements and model predictions for 10 g/L multicomponent brines from Salar de Atacama, Chile, under a constant current density of 2.5 mA cm^{-2} at pH (**A**) 7, (**B**) 5 and (**C**) 3, respectively.

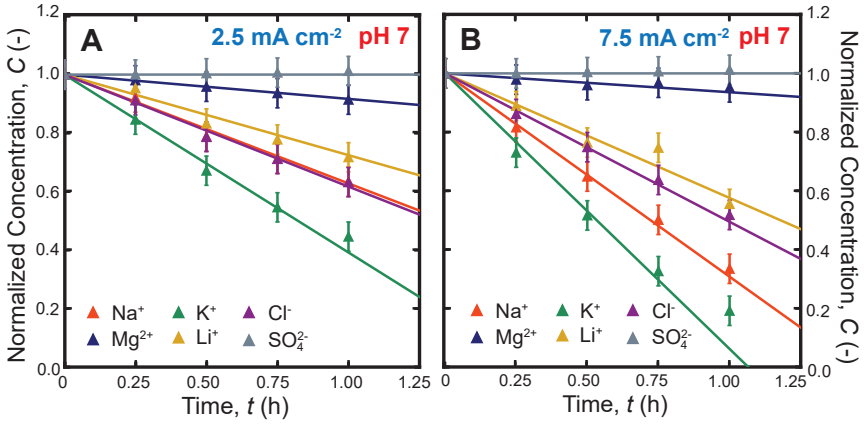

Supplementary Figure 3: Comparisons between the experimental measurements and model predictions for 30 g/L multicomponent brines from Salar de Atacama, Chile, under a constant at pH 7, for current density of (**A**) 2.5 and (**B**) 7.5 mA cm^{-2}, respectively.

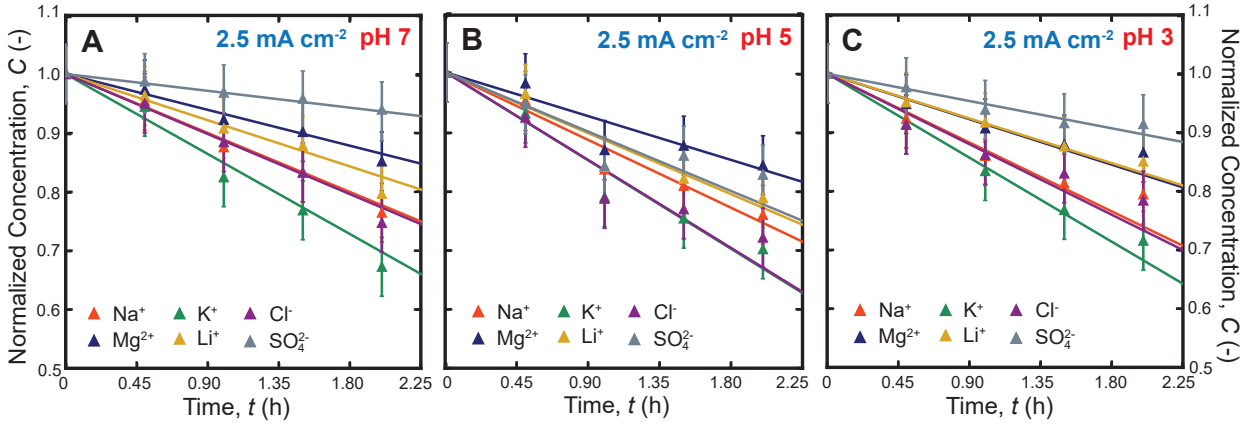

Supplementary Figure 4: Comparisons between the experimental measurements and model predictions for 70 g/L multicomponent brines from Salar de Atacama, Chile, under a constant current density of 2.5 mA cm^{-2} at pH (**A**) 7, (**B**) 5 and (**C**) 3, respectively.

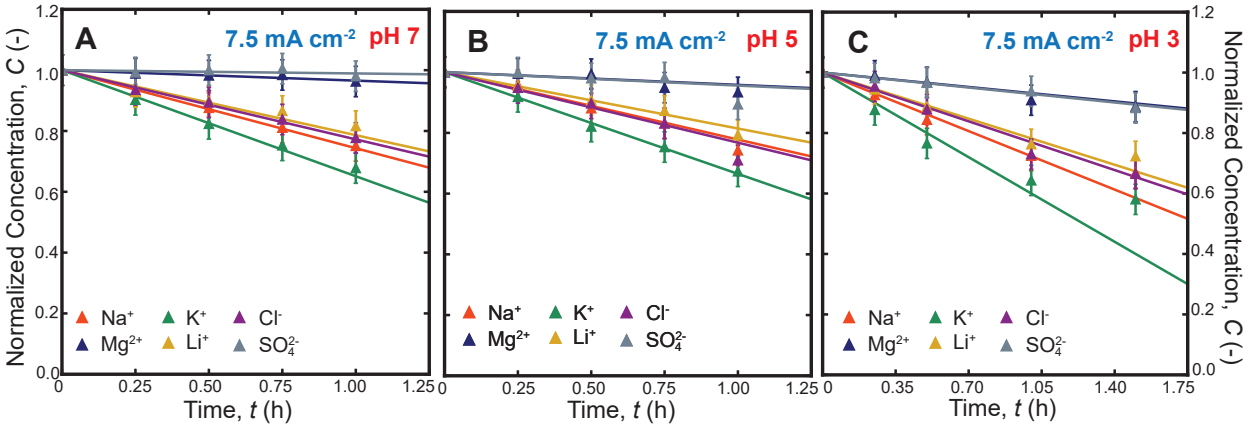

Supplementary Figure 5: Comparisons between the experimental measurements and model predictions for 70 g/L multicomponent brines from Salar de Atacama, Chile, under a constant current density of 7.5 mA cm^{-2} at pH (**A**) 7, (**B**) 5 and (**C**) 3, respectively.

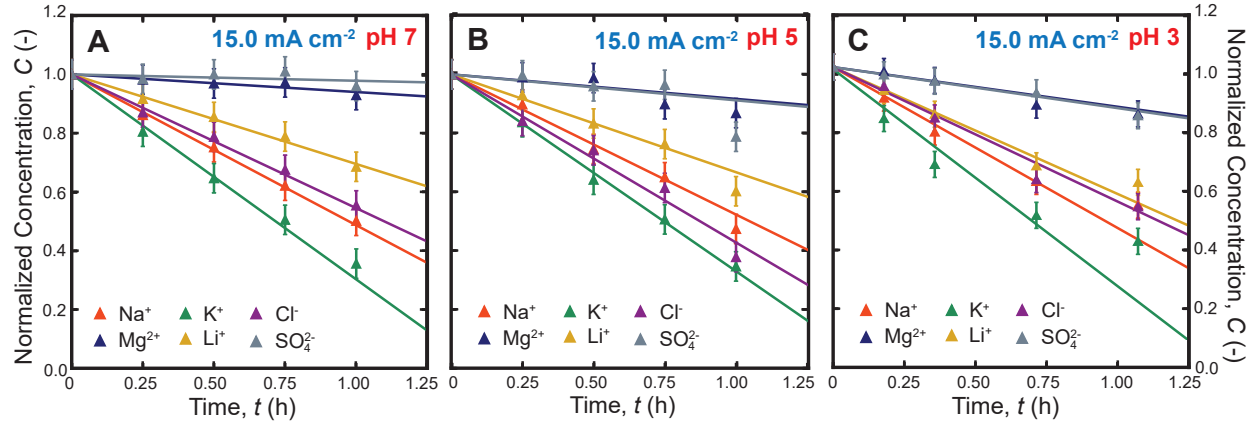

Supplementary Figure 6: Comparisons between the experimental measurements and model predictions for 70 g/L multicomponent brines from Salar de Atacama, Chile, under a constant current density of 15.0 mA cm^{-2} at pH (**A**) 7, (**B**) 5 and (**C**) 3, respectively.

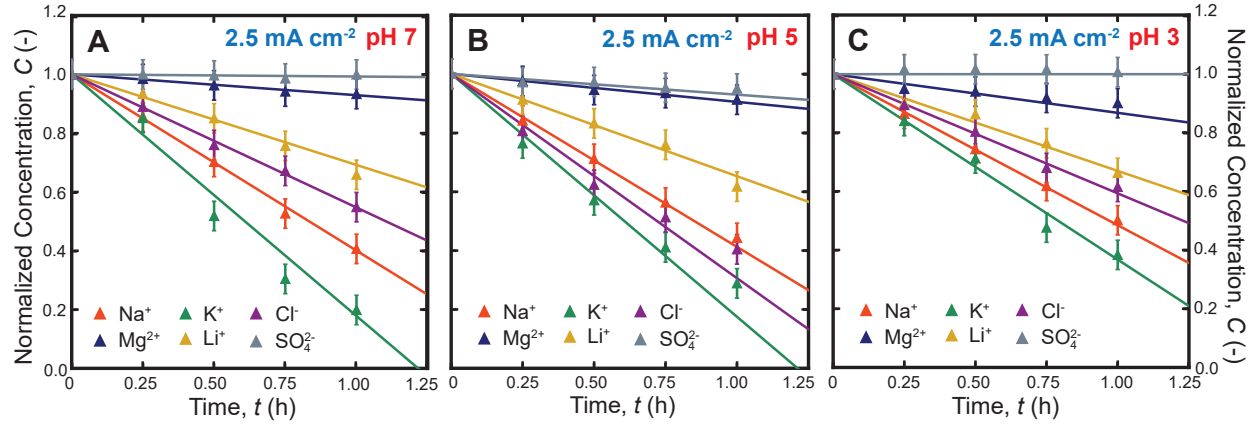

Supplementary Figure 7: Comparisons between the experimental measurements and model predictions for 10 g/L multicomponent brines from Qaidam Lake, China, under a constant current density of 2.5 mA cm^{-2} at pH (**A**) 7, (**B**) 5 and (**C**) 3, respectively.

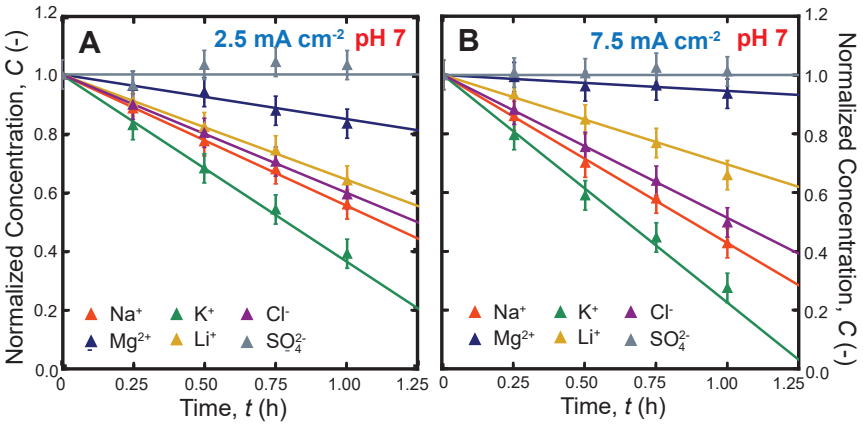

Supplementary Figure 8: Comparisons between the experimental measurements and model predictions for 30 g/L multicomponent brines from Qaidam Lake, China, under a constant at pH 7, for current density of (**A**) 2.5 and (**B**) 7.5 mA cm^{-2}, respectively.

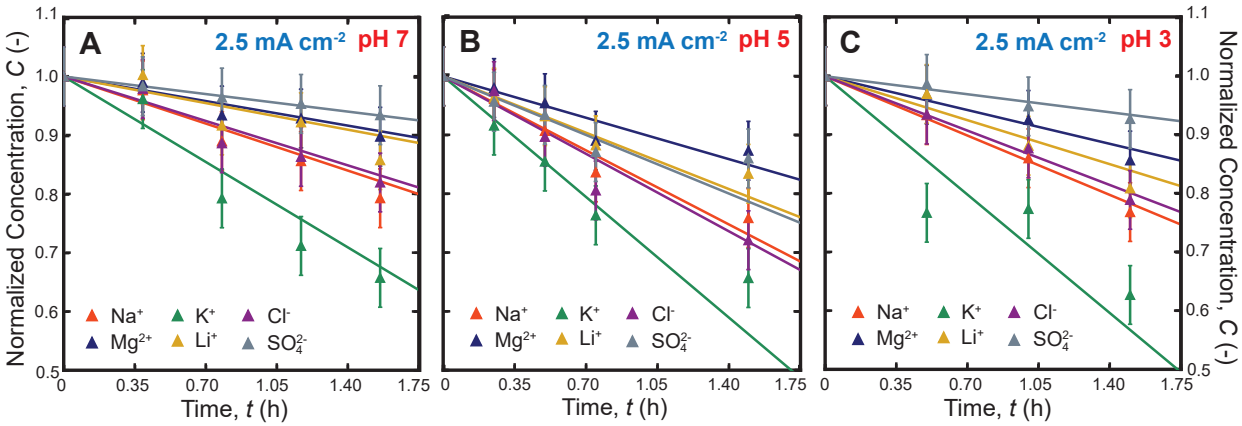

Supplementary Figure 9: Comparisons between the experimental measurements and model predictions for 70 g/L multicomponent brines from Qaidam Lake, China, under a constant current density of 2.5 mA cm^{-2} at pH (**A**) 7, (**B**) 5 and (**C**) 3, respectively.

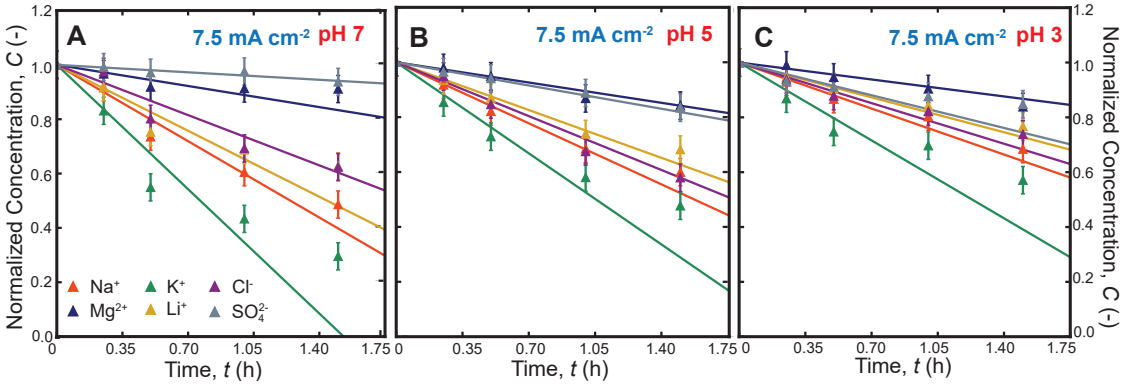

Supplementary Figure 10: Comparisons between the experimental measurements and model predictions for 70 g/L multicomponent brines from Qaidam Lake, China, under a constant current density of 7.5 mA cm^{-2} at pH (**A**) 7, (**B**) 5 and (**C**) 3, respectively.

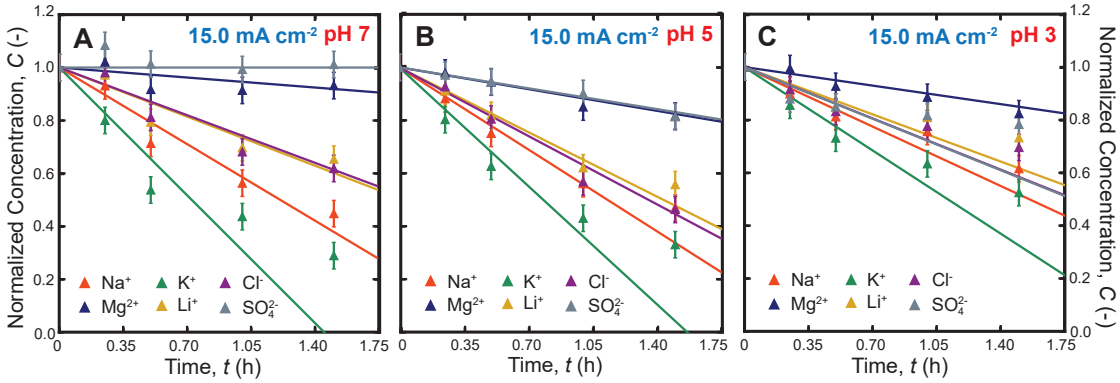

Supplementary Figure 11: Comparisons between the experimental measurements and model predictions for 70 g/L multicomponent brines from Qaidam Lake, China, under a constant current density of 15.0 mA cm^{-2} at pH (**A**) 7, (**B**) 5 and (**C**) 3, respectively.

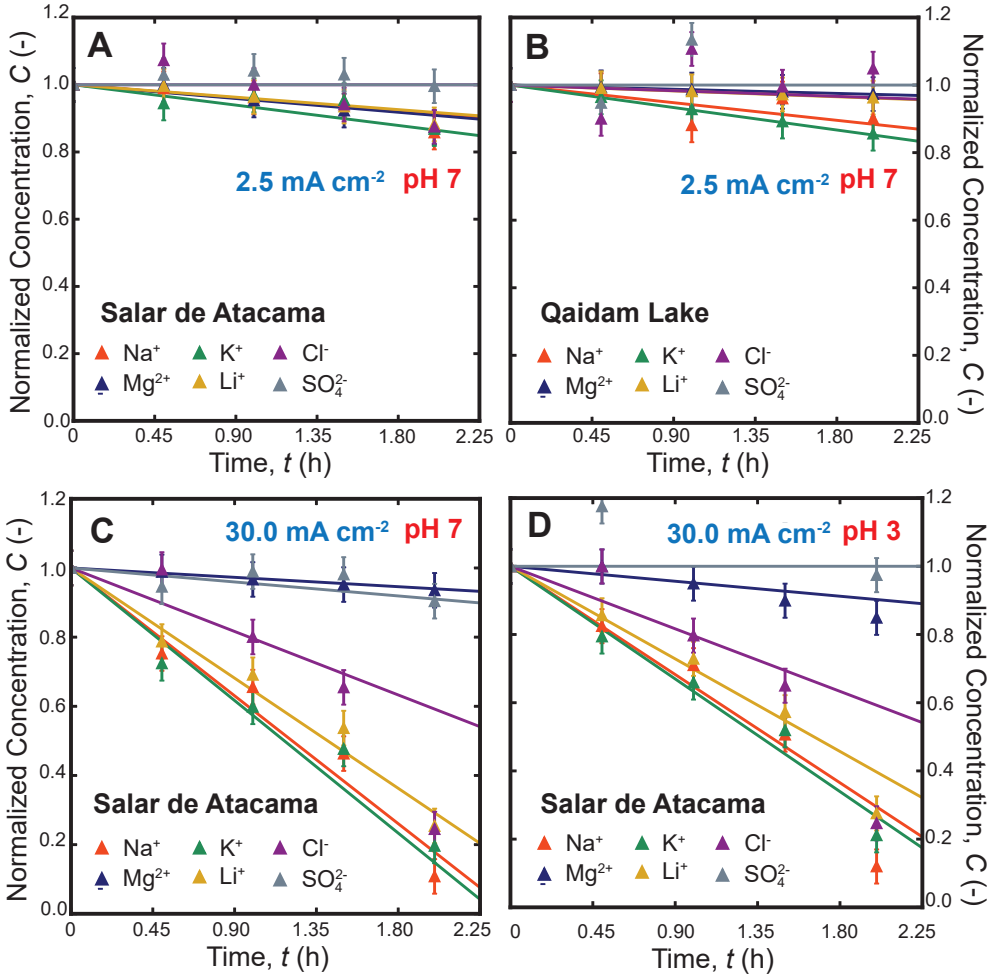

Supplementary Figure 12: Comparisons between the experimental measurements and model predictions for 250 g/L multicomponent brines from (**A**) Salar de Atacama, Chile and (**B**) Qaidam Lake, China, under a constant current density of 2.5 mA cm^{-2} at pH 7; corresponding results for 250 g/L multicomponent brine from Salar de Atacama, Chile, under a constant current density of 30.0 mA cm^{-2} at (**C**) pH 7 and (**D**) pH 3, respectively.

C Supplemental Analysis

C.1 Charge Density Impact on Donnan Exclusion

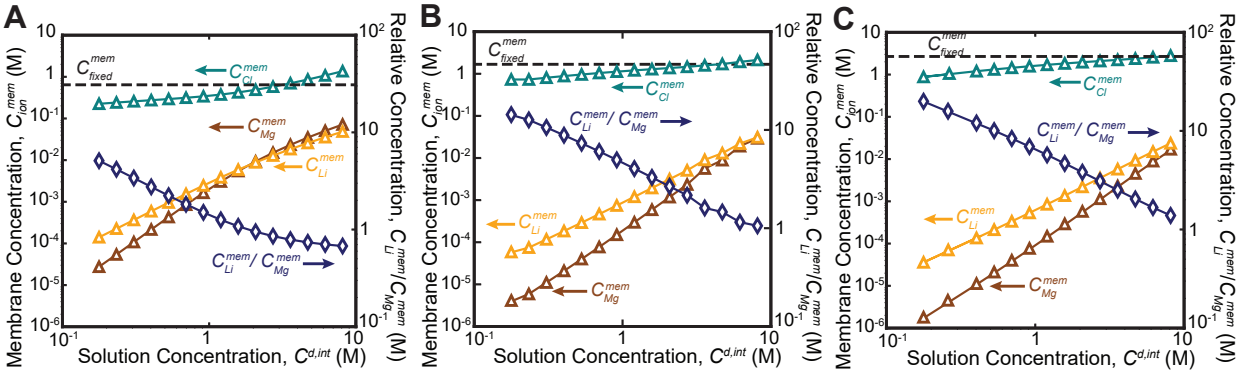

Supplementary Figure 13: Concentration of Li^+, Mg^{2+} and Cl^- ions within the PEI layer of the CEM for a constant volumetric charge density, as a function of the external solution concentration along the fluid-membrane interface. Relative concentrations of Li^+ to Mg^{2+} decay with increasing solution concentration, arising from weakening Donnan exclusion effects.[2] The volumetric charge densities of the PEI layer are (**A**) 0.5 M, (**B**) 1.68 M, and (**C**) 5.0 M, respectively, to simulate the effects of the lowered volumetric charge density with acid pre-treatment for salt-lake brine applications.

Our zeta potential measurements presented in Fig. 3C indicate that the interfacial potential of the diffuse layer decreases by approximately 41.7 %, likely as a result of a lowered volumetric charge density under low solution pH. This coincides with an increase in Mg^{2+} leakage by 18 %, and a decrease in the monovalent cation fluxes by 14 % or greater, suggesting that the weakening of Donnan exclusion is principal for the selectivity decline.

Using the terminology as defined in Figure 3D and E in the main manuscript, Eq. 14–16 in the SI are solved simultaneously to analyze the impact of the volumetric charge density on the monovalent selectivity of the CEM. Here, a CEM with volumetric charge densities of 0.50, 1.68 and 5.00 M are used to simulate the impacts of the solution pH on the charged moiety density of the PEI layer,[2,29] as illustrated in Supp. Figures 13A, B and C, respectively.

With a high volumetric charge density of 5.0 M, as observed in Supp. Figure 13C, a large Li^+/Mg^{2+} molar ratio of the partitioned ions exceeding 30 is obtained at 10 g L^{-1} TDS (0.35 M). While the partitioning selectivity decreases with increasing feed solution concentrations, a Li^+/Mg^{2+} molar ratio that is greater than parity is obtained even with salt-lake brine concentrations. When the

volumetric charge density is reduced from 1.68 to 0.5 M to mimic our zeta potential observations, the Li^+/Mg^{2+} molar ratio of the partitioned ions decreases drastically across the entire concentration range, and falls under parity once the solution concentration exceeds the 0.5 M. When the solution concentration exceeds the volumetric charge density of the CEM, more co-ions (i.e., Cl^-) will partition into the interstitial phase, and additional counter-ion partitioning (i.e., Li^+, Mg^{2+}) is necessary to maintain the electroneutrality condition. As a consequence, our model indicate that the resultant Donnan potential will attenuate, and more multivalent cations will be able to partition successfully into the CEM, reducing the effectiveness of Donnan exclusion of Mg^{2+} ions. Therefore, our numerical findings corroborate our empirical inference of the weakening of Donnan exclusion under low solution pH.

C.2 Composition Impacts on Monovalent Selectivity

In our prior NF publication, we observed that apparent Li/Mg separation factors may be overestimated by up to 40 % when the anionic composition of the feed solution is simplified to just one anion (either Cl^- or SO_4^{2-}).[30] This arises from transport coupling between the cations and anions, induced by electroneutrality constraints. For example, with Li^+ -Mg^{2+} -SO_4^{2-} feed solutions, the apparent Li^+ and Mg^{2+} rejection was significantly overestimated as a result of the poor permeability of SO_4^{2-} ions. When the Cl^-/SO_4^{2-} molar ratio was accurately replicated with the Li^+-Mg^{2+}-Cl^--SO_4^{2-} feed solutions, the absolute errors for Li/Mg separation factors fell under 15 %. Similar to our previous NF study, our ED experiments with binary cation feed solutions overpredict the Li/Mg separation factors by 50 to 250 %. Unlike NF, however, the errors in the Li/Mg separation factors remained large even when the Cl^-/SO_4^{2-} molar ratio was accurately replicated with the Li^+-Mg^{2+}-Cl^--SO_4^{2-} feed solutions. This result indicates that the other monovalent cations have an influence on the relative ionic flux between Li^+ and Mg^{2+}.

Similar to NF, the diluate and concentrate streams are still subjected to same electroneutrality constraint. In electrodialysis, however, the bulk anion and cation ions are transported separately through the AEM and CEM, and the two ion exchange membranes behave as separate conductors that are connected in series.[5] For a given current density, ED experiments with Li^+-Mg^{2+}-SO_4^{2-} (LMS) feed solutions will register a much greater SO_4^{2-} ion flux than that with Li^+-Mg^{2+}-Cl–SO_4^{2-}

(LMCS) solutions, albeit with a significantly amplified potential difference across the membrane stack due to the low conductance of SO_4^{2-} ions across the AEM. If the applied current density is equal in both experiments, the ion flux of SO_4^{2-} does not appear to present a significant barrier to the transport of the monovalent cations between the LMS and LMCS experiments. This is likely because the AEM is not perfectly monovalent selective and will allow SO_4^{2-} leakage when the potential difference across the AEM is sufficiently high.

On the other hand, if the AEM rejects SO_4^{2-} ions perfectly (hypothetical ideal monovalent selective AEM), then the ionic flux across the AEM would be negligible in experiments with Li^+-Mg^{2+}-SO_4^{2-} (LMS) feed solutions, and the ohmic resistance across the AEM would tend towards infinity. In this scenario, we would expect to see the same behavior in the Li/Mg separation factors as with NF, where the low transport rate of SO_4^{2-} limits the net ionic flux of Li^+ and Mg^{2+}. However, our AEMs are not perfectly selective, and significant SO_4^{2-} ion fluxes were measured with our LMS experiments.

C.3 Lithium Concentration in Salar de Atacama

In this section, we assess the implications of our research findings on the process duration and land area requirements for direct salt-lake lithium extraction. Currently, over 50 % of the global lithium supply originates from continental and geothermal brines, leveraging evaporitic technology for solution concentration.[31] Presently, the lithium-enriched hypersaline brines are pumped into evaporation ponds and concentrated by direct solar irradiation, over an average production cycle of two years.[32] Carbonates and phosphates of sodium and potassium are injected into the evaporation ponds when the solution concentrations of magnesium and lithium ions are close to their respective saturation indices.[33] The precipitated salts are subsequently collected and washed with fresh water.[31] The production dependence on evaporation ponds renders the lithium supply to be extremely price inelastic and slow to respond to the market demand. Further, only large flat areas in low humidity climates that are not prone to monsoon or seasonal changes are suitable to function as evaporation ponds. As a result, there are very few suitable flat lands that coincide geographically with lithium-rich aqueous deposits that can be exploited for direct lithium extraction.[33] With the appropriate selective IEM, an industrial-scale electrodialysis system can concentrate lithium in a

continuous process, potentially overcoming the reliance on evaporation ponds and access untapped lithium deposits for direct extraction.

The Salar de Atacama salt-lake in Chile produces 121,190 tones of lithium carbonate per year with 3000 km^2 of salt flat area.[31] Each production cycle takes approximately 2 years, and over 2.7 $\times 10^6$ m^3 of fresh water is consumed for solid salt isolation. On a molar basis, the Chilean salt-lake produces 8.99 $\times 10^6$ moles of Li on average per day, and the land area impact per mole of Li produced is 3.34 $\times 10^{-4}$ km^2 mol^{-1}. For electrodialysis, the land area requirement per mole of Li produced can be calculated with Eq. 20

$$\overline{A}_{Li} = \frac{\text{LAI } P_{ED}}{t_{Prod}\ J_{Li}\ A_{Mem}} \tag{20}$$

where $\overline{A}_{Li}$ (km^2 mol^{-1}) denotes the normalized land area requirement, LAI (km^2 GW^{-1}) denotes the land area impact per unit power, P_{ED} (GW) denotes the power consumed by the industrial-scale electrodialysis stack, t_{Prod} (h) denotes the daily production time, J_{Li} (mol m^{-2} h^{-1}) denotes the molar flux of Li, and A_{Mem} (m^2) denotes the total membrane area of the IEMs.

Here, we leverage our experimental results on the 250 g L^{-1} Chilean brines to project the energy and land area requirements for lithium extraction. An industrial-scale electrodialysis module comprising 100,000 cell pairs that is typically used for salt production is employed to estimate ED's performance.[9] To simulate DLE application, the diluate and concentrate stream compositions correspond to the salt-lake brine and a 0.1 M NaCl solution.[34] The land area impact of a photovoltaic solar farm to meet ED's electrical work requirement is calculated based on the survey by Palmer-Wilson et al.,[35] which incorporates the spatial demands arising from power generation, storage and transmission in a solar farm.

Assuming a 10 h daily production cycle, using existing monovalent selective CEMs driven by a current density of 30.0 mA cm^{-2}, our model indicates that over 7.70 $\times 10^6$ moles of Li can be extracted per day with a commercial-scale ED unit operation; the quantity of Li extracted from a single ED operation is over 85 % of the current capacity of Salar de Atacama. In a single stage, over 85.8 % of the dissolved Li can be extracted, and the product Li^+/Mg^+ ratio decreases by a factor of 6.58. Correspondingly, based on the land area impact survey, a solar farm operating for 10 h daily with a total footprint between 11.35 to 12.84 km^2 can generate sufficient electrical work to

power the continuous ED process.[35] The normalized land requirement ($\overline{A}_{Li}$) for ED is estimated to be between 1.21 $\times 10^{-6}$ to 1.67 $\times 10^{-6}$ km^2 mol^{-1}, which is over two orders of magnitude lower than the corresponding value obtained for the evaporation ponds at Salar de Atacama. The favorable results arise because the electrical work required for ion transport in ED is significantly lower than the latent heat consumed to vaporize water in a evaporation pond.[36]

D Experimental Data

Supplementary Table 5: Transient behavior of the normalized ion concentrations for Chilean brine at a total dissolved solid concentration of 10 g/L, solution pH of 7, under a current density of 2.5 mA cm^{-2}.

t (min)	Li^+ (-)	Mg^{2+} (-)	Na^+ (-)	K^+(-)	Cl^-(-)	SO_4^{2-}(-)
0	1.000	1.000	1.000	1.000	1.000	1.000
15	0.929	0.974	0.917	0.815	0.898	1.038
30	0.847	0.977	0.787	0.660	0.818	1.071
45	0.815	0.971	0.651	0.515	0.726	1.098
60	0.745	0.943	0.599	0.392	0.596	1.106
120	0.434	0.833	0.213	0.096	0.252	1.147

Supplementary Table 6: Transient behavior of the normalized ion concentrations for Chilean brine at a total dissolved solid concentration of 10 g/L, solution pH of 5, under a current density of 2.5 mA cm^{-2}.

t (min)	Li^+ (-)	Mg^{2+} (-)	Na^+ (-)	K^+(-)	Cl^-(-)	SO_4^{2-}(-)
0	1.000	1.000	1.000	1.000	1.000	1.000
15	0.925	0.984	0.876	0.771	0.826	0.981
30	0.877	0.969	0.765	0.594	0.701	0.988
45	0.791	0.950	0.648	0.448	0.540	0.980
60	0.710	0.908	0.523	0.324	0.422	0.941
120	0.292	0.811	0.131	0.072	0.115	0.906

Supplementary Table 7: Transient behavior of the normalized ion concentrations for Chilean brine at a total dissolved solid concentration of 10 g/L, solution pH of 3, under a current density of 2.5 mA cm^{-2}.

t (min)	Li^+ (-)	Mg^{2+} (-)	Na^+ (-)	K^+(-)	Cl^-(-)	SO_4^{2-}(-)
0	1.000	1.000	1.000	1.000	1.000	1.000
15	0.923	0.978	0.886	0.796	0.883	1.006
30	0.864	0.951	0.771	0.603	0.780	1.024
45	0.774	0.934	0.605	0.448	0.665	1.053
60	0.722	0.921	0.560	0.333	0.562	1.098
120	0.342	0.798	0.156	0.070	0.183	1.166

Supplementary Table 8: Transient behavior of the normalized ion concentrations for Chilean brine at a total dissolved solid concentration of 30 g/L, solution pH of 7, under a current density of 2.5 mA cm^{-2}.

t (min)	Li^+ (-)	Mg^{2+} (-)	Na^+ (-)	K^+(-)	Cl^-(-)	SO_4^{2-}(-)
0	1.000	1.000	1.000	1.000	1.000	1.000
15	0.953	0.980	0.921	0.846	0.912	1.245
30	0.833	0.958	0.788	0.671	0.786	1.203
45	0.778	0.936	0.712	0.546	0.711	1.285
60	0.717	0.914	0.634	0.446	0.632	1.298
90	0.553	0.892	0.456	0.272	0.454	1.221
120	0.413	0.870	0.310	0.137	0.321	1.107

Supplementary Table 9: Transient behavior of the normalized ion concentrations for Chilean brine at a total dissolved solid concentration of 30 g/L, solution pH of 7, under a current density of 7.5 mA cm^{-2}.

t (min)	Li^+ (-)	Mg^{2+} (-)	Na^+ (-)	K^+(-)	Cl^-(-)	SO_4^{2-}(-)
0	1.000	1.000	1.000	1.000	1.000	1.000
15	0.889	0.979	0.816	0.730	0.862	1.000
30	0.764	0.960	0.649	0.516	0.749	1.004
45	0.747	0.968	0.501	0.326	0.637	1.007
60	0.555	0.952	0.334	0.191	0.518	1.012
90	0.171	0.927	0.067	0.055	0.268	1.009
120	0.024	0.583	0.001	0.018	0.051	0.982

Supplementary Table 10: Transient behavior of the normalized ion concentrations for Chilean brine at a total dissolved solid concentration of 70 g/L, solution pH of 7, under a current density of 2.5 mA cm^{-2}.

t (min)	Li^+ (-)	Mg^{2+} (-)	Na^+ (-)	K^+(-)	Cl^-(-)	SO_4^{2-}(-)
0	1.000	1.000	1.000	1.000	1.000	1.000
30	0.963	0.973	0.954	0.944	0.950	0.985
60	0.907	0.922	0.876	0.825	0.884	0.965
90	0.878	0.901	0.832	0.768	0.833	0.955
120	0.796	0.851	0.764	0.672	0.747	0.937
150	0.767	0.829	0.736	0.624	0.716	0.932

Supplementary Table 11: Transient behavior of the normalized ion concentrations for Chilean brine at a total dissolved solid concentration of 70 g/L, solution pH of 5, under a current density of 2.5 mA cm^{-2}.

t (min)	Li^+ (-)	Mg^{2+} (-)	Na^+ (-)	K^+(-)	Cl^-(-)	SO_4^{2-}(-)
0	1.000	1.000	1.000	1.000	1.000	1.000
30	0.964	0.982	0.952	0.931	0.924	0.946
60	0.841	0.869	0.836	0.789	0.787	0.842
90	0.820	0.876	0.809	0.753	0.769	0.859
120	0.788	0.843	0.759	0.701	0.721	0.827
150	0.809	0.874	0.776	0.692	0.731	0.861

Supplementary Table 12: Transient behavior of the normalized ion concentrations for Chilean brine at a total dissolved solid concentration of 70 g/L, solution pH of 3, under a current density of 2.5 mA cm^{-2}.

t (min)	Li^+ (-)	Mg^{2+} (-)	Na^+ (-)	K^+(-)	Cl^-(-)	SO_4^{2-}(-)
0	1.000	1.000	1.000	1.000	1.000	1.000
30	0.951	0.948	0.923	0.914	0.913	0.977
60	0.917	0.907	0.860	0.834	0.862	0.939
90	0.876	0.879	0.813	0.768	0.830	0.916
120	0.850	0.866	0.794	0.716	0.784	0.914
150	0.832	0.858	0.747	0.690	0.768	0.917

Supplementary Table 13: Transient behavior of the normalized ion concentrations for Chilean brine at a total dissolved solid concentration of 70 g/L, solution pH of 7, under a current density of 7.5 mA cm^{-2}.

t (min)	Li^+ (-)	Mg^{2+} (-)	Na^+ (-)	K^+(-)	Cl^-(-)	SO_4^{2-}(-)
0	1.000	1.000	1.000	1.000	1.000	1.000
15	0.928	0.989	0.931	0.902	0.935	0.992
30	0.898	0.982	0.876	0.823	0.894	1.000
60	0.866	0.984	0.811	0.753	0.838	1.005
90	0.816	0.963	0.751	0.678	0.777	0.980
120	0.615	0.950	0.564	0.515	0.585	0.983

Supplementary Table 14: Transient behavior of the normalized ion concentrations for Chilean brine at a total dissolved solid concentration of 70 g/L, solution pH of 5, under a current density of 7.5 mA cm^{-2}.

t (min)	Li^+ (-)	Mg^{2+} (-)	Na^+ (-)	K^+(-)	Cl^-(-)	SO_4^{2-}(-)
0	1.000	1.000	1.000	1.000	1.000	1.000
15	0.955	0.995	0.958	0.919	0.948	0.998
30	0.907	0.994	0.881	0.821	0.897	0.980
60	0.873	0.949	0.832	0.753	0.831	0.982
90	0.793	0.934	0.742	0.673	0.710	0.894
120	0.742	0.875	0.675	0.602	0.641	0.912

Supplementary Table 15: Transient behavior of the normalized ion concentrations for Chilean brine at a total dissolved solid concentration of 70 g/L, solution pH of 3, under a current density of 7.5 mA cm^{-2}.

t (min)	Li^+ (-)	Mg^{2+} (-)	Na^+ (-)	K^+(-)	Cl^-(-)	SO_4^{2-}(-)
0	1.000	1.000	1.000	1.000	1.000	1.000
15	0.944	0.990	0.926	0.876	0.954	0.981
30	0.887	0.968	0.844	0.766	0.878	0.966
60	0.763	0.909	0.725	0.643	0.730	0.938
90	0.723	0.887	0.668	0.581	0.665	0.883
120	0.671	0.860	0.608	0.523	0.601	0.861

Supplementary Table 16: Transient behavior of the normalized ion concentrations for Chilean brine at a total dissolved solid concentration of 70 g/L, solution pH of 7, under a current density of 15.0 mA cm^{-2}.

t (min)	Li^+ (-)	Mg^{2+} (-)	Na^+ (-)	K^+(-)	Cl^-(-)	SO_4^{2-}(-)
0	1.000	1.000	1.000	1.000	1.000	1.000
15	0.917	0.982	0.862	0.805	0.871	0.985
30	0.855	0.969	0.752	0.647	0.788	1.000
45	0.788	0.973	0.621	0.505	0.676	1.010
60	0.686	0.929	0.502	0.356	0.554	0.960
120	0.271	0.903	0.129	0.031	0.171	0.967

Supplementary Table 17: Transient behavior of the normalized ion concentrations for Chilean brine at a total dissolved solid concentration of 70 g/L, solution pH of 5, under a current density of 15.0 mA cm^{-2}.

t (min)	Li^+ (-)	Mg^{2+} (-)	Na^+ (-)	K^+(-)	Cl^-(-)	SO_4^{2-}(-)
0	1.000	1.000	1.000	1.000	1.000	1.000
15	0.929	0.990	0.898	0.837	0.841	0.997
30	0.833	0.987	0.746	0.641	0.742	0.959
45	0.763	0.898	0.650	0.506	0.614	0.965
60	0.602	0.868	0.474	0.346	0.378	0.788
120	0.500	0.751	0.342	0.203	0.245	0.823

Supplementary Table 18: Transient behavior of the normalized ion concentrations for Chilean brine at a total dissolved solid concentration of 70 g/L, solution pH of 3, under a current density of 15.0 mA cm^{-2}.

t (min)	Li^+ (-)	Mg^{2+} (-)	Na^+ (-)	K^+(-)	Cl^-(-)	SO_4^{2-}(-)
0	1.000	1.000	1.000	1.000	1.000	1.000
15	0.911	0.983	0.881	0.802	0.926	0.970
30	0.819	0.949	0.750	0.626	0.804	0.946
60	0.621	0.854	0.560	0.430	0.567	0.901
90	0.557	0.820	0.469	0.330	0.463	0.813
120	0.474	0.775	0.374	0.239	0.360	0.779

Supplementary Table 19: Transient behavior of the normalized ion concentrations for Chilean brine at a total dissolved solid concentration of 250 g/L, solution pH of 7, under a current density of 2.5 mA cm^{-2}.

t (min)	Li^+ (-)	Mg^{2+} (-)	Na^+ (-)	K^+(-)	Cl^-(-)	SO_4^{2-}(-)
0	1.000	1.000	1.000	1.000	1.000	1.000
30	0.996	1.000	0.989	0.944	1.073	1.029
60	0.964	0.953	0.962	0.968	0.999	1.041
90	0.935	0.923	0.952	0.954	0.941	1.030
120	0.882	0.873	0.858	0.868	0.875	0.996
150	0.861	0.888	0.873	0.816	0.872	1.002

Supplementary Table 20: Transient behavior of the normalized ion concentrations for Chilean brine at a total dissolved solid concentration of 250 g/L, solution pH of 7, under a current density of 30.0 mA cm^{-2}.

t (min)	Li^+ (-)	Mg^{2+} (-)	Na^+ (-)	K^+(-)	Cl^-(-)	SO_4^{2-}(-)
0	1.000	1.000	1.000	1.000	1.000	1.000
30	0.787	0.989	0.753	0.724	0.996	0.946
60	0.691	0.967	0.656	0.599	0.800	0.990
90	0.537	0.952	0.463	0.477	0.655	0.981
120	0.254	0.935	0.108	0.196	0.245	0.904
150	0.142	0.919	0.020	0.011	0.135	0.957

Supplementary Table 21: Transient behavior of the normalized ion concentrations for Chilean brine at a total dissolved solid concentration of 250 g/L, solution pH of 3, under a current density of 30.0 mA cm^{-2}.

t (min)	Li^+ (-)	Mg^{2+} (-)	Na^+ (-)	K^+(-)	Cl^-(-)	SO_4^{2-}(-)
0	1.000	1.000	1.000	1.000	1.000	1.000
30	0.856	0.999	0.825	0.794	0.999	1.176
60	0.729	0.949	0.710	0.659	0.797	1.250
90	0.572	0.899	0.506	0.519	0.650	1.179
120	0.275	0.849	0.120	0.211	0.246	0.974
150	0.152	0.799	0.022	0.012	0.134	1.011

Supplementary Table 22: Transient behavior of the normalized ion concentrations for Chinese brine at a total dissolved solid concentration of 10 g/L, solution pH of 7, under a current density of 2.5 mA cm^{-2}.

t (min)	Li^+ (-)	Mg^{2+} (-)	Na^+ (-)	K^+(-)	Cl^-(-)	SO_4^{2-}(-)
0	1.000	1.000	1.000	1.000	1.000	1.000
15	0.933	0.984	0.856	0.851	0.890	0.999
30	0.850	0.962	0.702	0.518	0.759	0.996
45	0.757	0.941	0.526	0.304	0.672	0.986
60	0.658	0.933	0.406	0.199	0.548	0.999
90	0.393	0.886	0.175	0.100	0.337	0.998
120	0.077	0.766	0.004	0.023	0.144	0.983

Supplementary Table 23: Transient behavior of the normalized ion concentrations for Chinese brine at a total dissolved solid concentration of 10 g/L, solution pH of 5, under a current density of 2.5 mA cm^{-2}.

t (min)	Li^+ (-)	Mg^{2+} (-)	Na^+ (-)	K^+(-)	Cl^-(-)	SO_4^{2-}(-)
0	1.000	1.000	1.000	1.000	1.000	1.000
15	0.912	0.976	0.841	0.764	0.806	0.971
30	0.832	0.945	0.712	0.571	0.623	0.972
45	0.759	0.935	0.563	0.411	0.513	0.953
60	0.617	0.912	0.443	0.288	0.404	0.950
90	0.413	0.870	0.207	0.125	0.235	0.916
120	0.127	0.805	0.033	0.031	0.119	0.903

Supplementary Table 24: Transient behavior of the normalized ion concentrations for Chinese brine at a total dissolved solid concentration of 10 g/L, solution pH of 3, under a current density of 2.5 mA cm^{-2}.

t (min)	Li^+ (-)	Mg^{2+} (-)	Na^+ (-)	K^+(-)	Cl^-(-)	SO_4^{2-}(-)
0	1.000	1.000	1.000	1.000	1.000	1.000
15	0.901	0.950	0.865	0.840	0.895	1.017
30	0.863	0.940	0.744	0.713	0.804	1.017
45	0.765	0.919	0.618	0.477	0.680	1.016
60	0.663	0.901	0.502	0.384	0.615	1.007
90	0.446	0.902	0.267	0.123	0.389	1.004
120	0.119	0.833	0.059	0.018	0.198	1.006

Supplementary Table 25: Transient behavior of the normalized ion concentrations for Chinese brine at a total dissolved solid concentration of 30 g/L, solution pH of 7, under a current density of 2.5 mA cm^{-2}.

t (min)	Li^+ (-)	Mg^{2+} (-)	Na^+ (-)	K^+(-)	Cl^-(-)	SO_4^{2-}(-)
0	1.000	1.000	1.000	1.000	1.000	1.000
15	0.906	0.961	0.883	0.826	0.896	0.962
30	0.819	0.939	0.771	0.677	0.800	1.133
45	0.740	0.875	0.674	0.536	0.701	1.143
60	0.636	0.831	0.554	0.384	0.588	1.132
90	0.464	0.787	0.367	0.215	0.411	1.062
120	0.298	0.765	0.206	0.087	0.255	1.107

Supplementary Table 26: Transient behavior of the normalized ion concentrations for Chinese brine at a total dissolved solid concentration of 30 g/L, solution pH of 7, under a current density of 7.5 mA cm^{-2}.

t (min)	Li^+ (-)	Mg^{2+} (-)	Na^+ (-)	K^+(-)	Cl^-(-)	SO_4^{2-}(-)
0	1.000	1.000	1.000	1.000	1.000	1.000
15	0.934	0.993	0.860	0.796	0.882	1.008
30	0.848	0.961	0.701	0.590	0.755	1.006
45	0.768	0.964	0.580	0.447	0.640	1.025
60	0.659	0.936	0.427	0.275	0.498	1.012
120	0.064	0.815	0.040	0.055	0.056	0.959

Supplementary Table 27: Transient behavior of the normalized ion concentrations for Chinese brine at a total dissolved solid concentration of 70 g/L, solution pH of 7, under a current density of 2.5 mA cm^{-2}.

t (min)	Li^+ (-)	Mg^{2+} (-)	Na^+ (-)	K^+(-)	Cl^-(-)	SO_4^{2-}(-)
0	1.000	1.000	1.000	1.000	1.000	1.000
30	1.003	0.989	0.977	0.962	0.979	0.983
60	0.917	0.934	0.890	0.793	0.886	0.964
90	0.922	0.929	0.856	0.712	0.863	0.953
120	0.858	0.898	0.793	0.657	0.820	0.934
180	0.816	0.868	0.716	0.600	0.747	0.934

Supplementary Table 28: Transient behavior of the normalized ion concentrations for Chinese brine at a total dissolved solid concentration of 70 g/L, solution pH of 5, under a current density of 2.5 mA cm^{-2}.

t (min)	Li^+ (-)	Mg^{2+} (-)	Na^+ (-)	K^+(-)	Cl^-(-)	SO_4^{2-}(-)
0	1.000	1.000	1.000	1.000	1.000	1.000
15	0.964	0.980	0.962	0.916	0.975	0.957
30	0.932	0.954	0.907	0.855	0.897	0.935
45	0.883	0.890	0.837	0.764	0.806	0.871
90	0.834	0.873	0.759	0.657	0.721	0.860
120	0.857	0.904	0.757	0.621	0.734	0.915
150	0.709	0.785	0.621	0.499	0.566	0.785

Supplementary Table 29: Transient behavior of the normalized ion concentrations for Chinese brine at a total dissolved solid concentration of 70 g/L, solution pH of 3, under a current density of 2.5 mA cm^{-2}.

t (min)	Li^+ (-)	Mg^{2+} (-)	Na^+ (-)	K^+(-)	Cl^-(-)	SO_4^{2-}(-)
0	1.000	1.000	1.000	1.000	1.000	1.000
30	0.970	0.969	0.934	0.767	0.934	0.987
60	0.881	0.926	0.860	0.774	0.877	0.949
90	0.809	0.856	0.768	0.627	0.789	0.927
120	0.756	0.807	0.698	0.574	0.730	0.901
180	0.669	0.749	0.594	0.428	0.631	0.850

Supplementary Table 30: Transient behavior of the normalized ion concentrations for Chinese brine at a total dissolved solid concentration of 70 g/L, solution pH of 7, under a current density of 7.5 mA cm^{-2}.

t (min)	Li^+ (-)	Mg^{2+} (-)	Na^+ (-)	K^+(-)	Cl^-(-)	SO_4^{2-}(-)
0	1.000	1.000	1.000	1.000	1.000	1.000
15	0.918	0.966	0.916	0.831	0.975	0.992
30	0.752	0.918	0.735	0.549	0.802	0.971
60	0.687	0.913	0.605	0.433	0.692	0.976
90	0.627	0.911	0.486	0.295	0.624	0.937
120	0.389	0.851	0.254	0.128	0.414	0.929

Supplementary Table 31: Transient behavior of the normalized ion concentrations for Chinese brine at a total dissolved solid concentration of 70 g/L, solution pH of 5, under a current density of 7.5 mA cm^{-2}.

t (min)	Li^+ (-)	Mg^{2+} (-)	Na^+ (-)	K^+(-)	H_3O^+(-)	Cl^-(-)	SO_4^{2-}(-)
0	1.000	1.000	1.000	1.000	1.000	1.000	1.000
15	0.935	0.979	0.917	0.854	0.722	0.948	0.964
30	0.870	0.949	0.821	0.729	0.560	0.846	0.941
60	0.738	0.868	0.685	0.580	0.450	0.675	0.888
90	0.682	0.842	0.599	0.477	0.326	0.579	0.834
120	0.646	0.831	0.546	0.411	0.216	0.528	0.840

Supplementary Table 32: Transient behavior of the normalized ion concentrations for Chinese brine at a total dissolved solid concentration of 70 g/L, solution pH of 3, under a current density of 7.5 mA cm^{-2}.

t (min)	Li^+ (-)	Mg^{2+} (-)	Na^+ (-)	K^+(-)	Cl^-(-)	SO_4^{2-}(-)
0	1.000	1.000	1.000	1.000	1.000	1.000
15	0.945	0.990	0.929	0.868	0.938	0.931
30	0.903	0.946	0.866	0.747	0.878	0.911
60	0.842	0.904	0.803	0.697	0.821	0.876
90	0.767	0.838	0.684	0.571	0.738	0.848
120	0.672	0.755	0.594	0.456	0.633	0.818

Supplementary Table 33: Transient behavior of the normalized ion concentrations for Chinese brine at a total dissolved solid concentration of 70 g/L, solution pH of 7, under a current density of 15.0 mA cm^{-2}.

t (min)	Li^+ (-)	Mg^{2+} (-)	Na^+ (-)	K^+(-)	Cl^-(-)	SO_4^{2-}(-)
0	1.000	1.000	1.000	1.000	1.000	1.000
15	0.971	1.020	0.931	0.800	0.980	1.084
30	0.793	0.917	0.713	0.537	0.811	1.013
60	0.696	0.914	0.563	0.437	0.681	0.993
90	0.654	0.932	0.448	0.289	0.618	1.011
120	0.344	0.872	0.192	0.104	0.387	0.960
150	0.083	0.812	0.029	0.020	0.223	0.970

Supplementary Table 34: Transient behavior of the normalized ion concentrations for Chinese brine at a total dissolved solid concentration of 70 g/L, solution pH of 5, under a current density of 15.0 mA cm^{-2}.

t (min)	Li^+ (-)	Mg^{2+} (-)	Na^+ (-)	K^+(-)	Cl^-(-)	SO_4^{2-}(-)
0	1.000	1.000	1.000	1.000	1.000	1.000
15	0.911	0.979	0.881	0.802	0.926	0.970
30	0.819	0.944	0.750	0.626	0.804	0.946
60	0.621	0.850	0.560	0.430	0.567	0.901
90	0.557	0.816	0.469	0.330	0.463	0.813
120	0.474	0.772	0.374	0.239	0.360	0.779
150	0.389	0.722	0.278	0.171	0.271	0.726

Supplementary Table 35: Transient behavior of the normalized ion concentrations for Chinese brine at a total dissolved solid concentration of 70 g/L, solution pH of 3, under a current density of 15.0 mA cm^{-2}.

t (min)	Li^+ (-)	Mg^{2+} (-)	Na^+ (-)	K^+(-)	Cl^-(-)	SO_4^{2-}(-)
0	1.000	1.000	1.000	1.000	1.000	1.000
15	0.912	0.994	0.898	0.855	0.914	0.783
30	0.849	0.927	0.811	0.731	0.831	1.160
60	0.809	0.886	0.756	0.634	0.775	0.849
90	0.732	0.823	0.615	0.525	0.696	0.879
120	0.604	0.713	0.509	0.360	0.553	1.208
150	0.464	0.599	0.358	0.193	0.432	1.154

Supplementary Table 36: Transient behavior of the normalized ion concentrations for Chinese brine at a total dissolved solid concentration of 250 g/L, solution pH of 7, under a current density of 2.5 mA cm^{-2}.

t (min)	Li^+ (-)	Mg^{2+} (-)	Na^+ (-)	K^+(-)	Cl^-(-)	SO_4^{2-}(-)
0	1.000	1.000	1.000	1.000	1.000	1.000
30	0.991	0.993	0.985	0.964	0.900	0.947
60	0.981	0.987	0.881	0.928	1.107	1.134
90	0.972	0.980	0.960	0.892	0.995	1.193
120	0.963	0.973	0.901	0.856	1.048	1.160
150	0.953	0.967	0.878	0.806	1.068	1.136

Supplementary Table 37: Transient behavior of the normalized ion concentrations for dual cation (Li^+ - Mg^{2+} - Cl^-, abbreviated as LMC) brine at a total dissolved solid concentration of 0.35 M, solution pH of 7, under a current density of 2.5 mA cm^{-2}.

t (min)	Li^+ (-)	Mg^{2+} (-)	Cl^-(-)	SO_4^{2-}(-)
0	1.000	1.000	1.000	0.00
15	0.755	0.985	0.900	0.00
30	0.513	0.947	0.819	0.00
45	0.283	0.931	0.751	0.00
60	0.106	0.899	0.674	0.00
90	0.015	0.754	0.542	0.00
120	0.009	0.598	0.420	0.00

Supplementary Table 38: Transient behavior of the normalized ion concentrations for dual cation (Li^+ - Mg^{2+} - Cl^- - SO_4^{2-}, abbreviated as LMCS) brine at a total dissolved solid concentration of 0.35 M, solution pH of 7, under a current density of 2.5 mA cm^{-2}.

t (min)	Li^+ (-)	Mg^{2+} (-)	Cl^-(-)	SO_4^{2-}(-)
0	1.000	1.000	1.000	1.000
15	0.744	0.983	0.905	1.009
30	0.451	0.976	0.812	0.987
45	0.257	0.949	0.752	0.992
60	0.082	0.909	0.685	0.991
90	0.019	0.770	0.536	0.997
120	0.014	0.627	0.418	0.986

Supplementary Table 39: Transient behavior of the normalized ion concentrations for dual cation (Li^+ - Mg^{2+} - Cl^- - SO_4^{2-}, abbreviated as LMCS) brine at a total dissolved solid concentration of 0.35 M, solution pH of 3, under a current density of 2.5 mA cm^{-2}.

t (min)	Li^+ (-)	Mg^{2+} (-)	Cl^-(-)	SO_4^{2-}(-)
0	1.000	1.000	1.000	1.000
15	0.718	0.980	0.893	1.017
30	0.459	0.953	0.811	1.017
45	0.213	0.935	0.718	1.016
60	0.069	0.875	0.646	1.007
90	0.016	0.713	0.500	1.004
120	0.012	0.564	0.376	1.006

Supplementary Table 40: Compiled ion transport numbers for the Chilean and Chinese salt-lake brine experiments.

Composition (-)	Concentration (g/L)	Solution pH (-)	Current Density (mA/cm^2)	Species Transport Number (-)					
				Li^+	Mg^{2+}	Na^+	K^+	Cl^-	SO_4^{2-}
Chile	10	3	2.5	1.429E-02	1.452E-02	3.855E-01	9.380E-02	4.960E-01	6.506E-08
Chile	10	5	2.5	1.143E-02	9.708E-03	3.249E-01	8.113E-02	5.702E-01	2.686E-03
Chile	10	7	2.5	1.570E-02	1.167E-02	3.876E-01	9.697E-02	4.964E-01	1.305E-08
Chile	30	7	2.5	1.529E-02	1.638E-02	3.670E-01	9.160E-02	5.104E-01	6.508E-08
Chile	30	7	7.5	1.536E-02	8.243E-03	4.453E-01	9.216E-02	4.393E-01	3.244E-07
Chile	70	3	2.5	1.331E-02	4.780E-02	3.605E-01	6.712E-02	4.993E-01	1.196E-02
Chile	70	3	7.5	1.818E-02	2.006E-02	4.061E-01	8.958E-02	4.574E-01	8.675E-03
Chile	70	3	15.0	1.817E-02	2.004E-02	4.055E-01	8.943E-02	4.582E-01	8.639E-03
Chile	70	5	2.5	1.594E-02	4.045E-02	3.118E-01	6.203E-02	5.469E-01	2.285E-02
Chile	70	5	7.5	1.356E-02	1.379E-02	3.641E-01	8.383E-02	5.150E-01	6.057E-03
Chile	70	5	15.0	1.730E-02	1.199E-02	3.417E-01	7.322E-02	5.542E-01	5.290E-03
Chile	70	7	2.5	1.605E-02	4.397E-02	3.605E-01	7.461E-02	4.963E-01	8.603E-03
Chile	70	7	7.5	1.369E-02	1.085E-02	4.025E-01	8.348E-02	4.827E-01	1.419E-03
Chile	70	7	15.0	1.906E-02	9.507E-03	4.053E-01	8.406E-02	4.860E-01	1.428E-03
Chile	250	7	2.5	1.439E-02	1.537E-02	3.798E-01	9.126E-02	4.920E-01	5.423E-07
Chile	250	7	30.0	2.727E-02	7.667E-03	5.255E-01	8.272E-02	3.520E-01	4.800E-03
Chile	250	3	30.0	2.609E-02	1.397E-02	5.066E-01	8.004E-02	3.947E-01	6.634E-08
China	10	3	2.5	3.847E-03	7.114E-02	4.098E-01	2.356E-02	4.993E-01	6.629E-08
China	10	5	2.5	2.849E-03	3.606E-02	3.288E-01	2.162E-02	5.993E-01	1.146E-02
China	10	7	2.5	3.244E-03	3.456E-02	4.307E-01	2.765E-02	5.023E-01	1.552E-03
China	30	7	2.5	5.798E-03	8.531E-02	3.698E-01	2.426E-02	5.150E-01	3.257E-07
China	30	7	7.5	4.267E-03	2.640E-02	4.098E-01	2.554E-02	5.385E-01	6.936E-08
China	70	3	2.5	4.667E-03	1.291E-01	3.337E-01	3.049E-02	4.727E-01	2.936E-02
China	70	3	7.5	4.911E-03	8.597E-02	3.432E-01	2.661E-02	4.685E-01	7.082E-02
China	70	3	15.0	5.214E-03	7.367E-02	3.476E-01	2.230E-02	4.637E-01	8.752E-02
China	70	5	2.5	4.333E-03	1.145E-01	3.016E-01	2.250E-02	4.879E-01	6.924E-02
China	70	5	7.5	5.309E-03	8.106E-02	3.592E-01	2.455E-02	4.901E-01	3.969E-02
China	70	5	15.0	5.665E-03	6.861E-02	3.806E-01	2.520E-02	4.918E-01	2.813E-02
China	70	7	2.5	3.537E-03	1.175E-01	3.315E-01	2.757E-02	4.840E-01	3.586E-02
China	70	7	7.5	7.014E-03	8.086E-02	4.300E-01	3.209E-02	4.378E-01	1.219E-02
China	70	7	15.0	5.831E-03	4.271E-02	4.819E-01	3.683E-02	4.637E-01	3.432E-07
China	250	7	2.5	4.753E-03	1.220E-01	7.586E-01	4.430E-02	3.761E-01	4.411E-07

References

(1) Ahdab, Y. D.; Rehman, D.; Lienhard, J. H. Brackish water desalination for greenhouses: Improving groundwater quality for irrigation using monovalent selective electrodialysis reversal. *Journal of Membrane Science* **2020**, *610*, 118072.

(2) Fan, H.; Yip, N. Y. Elucidating conductivity-permselectivity tradeoffs in electrodialysis and reverse electrodialysis by structure-property analysis of ion-exchange membranes. *Journal of Membrane Science* **2019**, *573*, 668–681.

(3) Yaroshchuk, A.; Bruening, M. L.; Zholkovskiy, E. Modelling nanofiltration of electrolyte solutions. *Advances in Colloid and Interface Science* **2019**, *268*, 39–63.

(4) Foo, Z. H.; Rehman, D.; Coombs, O. Z.; Deshmukh, A.; Lienhard, J. H. Multicomponent Fickian solution-diffusion model for osmotic transport through membranes. *Journal of Membrane Science* **2021**, *640*, 119819.

(5) Rehman, D.; Ahdab, Y. D.; Lienhard, J. H. Monovalent selective electrodialysis: Modelling multi-ionic transport across selective membranes. *Water Research* **2021**, *199*, 117171.

(6) Luo, T.; Abdu, S.; Wessling, M. Selectivity of ion exchange membranes: A review. *Journal of Membrane Science* **2018**, *555*, 429–454.

(7) Kingsbury, R. S.; Coronell, O. Modeling and validation of concentration dependence of ion exchange membrane permselectivity: Significance of convection and Manning's counter-ion condensation theory. *Journal of Membrane Science* **2021**, *620*, 118411.

(8) Kingsbury, R. S.; Zhu, S.; Flotron, S.; Coronell, O. Microstructure Determines Water and Salt Permeation in Commercial Ion-Exchange Membranes. *ACS Applied Materials & Interfaces* **2018**, *10*, 39745–39756.

(9) McGovern, R. K.; Weiner, A. M.; Sun, L.; Chambers, C. G.; Zubair, S. M.; Lienhard, J. H. On the cost of electrodialysis for the desalination of high salinity feeds. *Applied Energy* **2014**, *136*, 649–661.

(10) Strathmann, H. *Ion-exchange membrane separation processes*; Elsevier, 2004.

(11) Wenten, I. G.; Khoiruddin, K.; Alkhadra, M. A.; Tian, H.; Bazant, M. Z. Novel ionic separation mechanisms in electrically driven membrane processes. *Advances in Colloid and Interface Science* **2020**, *284*, 102269.

(12) Kamcev, J.; Galizia, M.; Benedetti, F. M.; Jang, E.-S.; Paul, D. R.; Freeman, B. D.; Manning, G. S. Partitioning of mobile ions between ion exchange polymers and aqueous salt solutions: importance of counter-ion condensation †. *Physical Chemistry Chemical Physics* **2016**, *18*, 6021.

(13) Fan, H.; Huang, Y.; Billinge, I. H.; Bannon, S. M.; Geise, G. M.; Yip, N. Y. Counterion Mobility in Ion-Exchange Membranes: Spatial Effect and Valency-Dependent Electrostatic Interaction. *ACS ES&T Engineering* **2022**, *2*, 1274–1286.

(14) Kamcev, J.; Paul, D. R.; Freeman, B. D. Ion activity coefficients in ion exchange polymers: Applicability of Manning's counterion condensation theory. *Macromolecules* **2015**, *48*, 8011–8024.

(15) Kim, H. T.; Frederick, W. J. Evaluation of Pitzer Ion Interaction Parameters of Aqueous Electrolytes at 25°C. 1. Single Salt Parameters. *Journal of Chemical and Engineering Data* **1988**, *33*, 177–184.

(16) Kim, H. T.; Frederick, W. J. Evaluation of pitzer ion interaction parameters of aqueous mixed electrolyte solutions at 25 °C. 2. Ternary mixing parameters. *Journal of Chemical and Engineering Data* **1988**, *33*, 278–283.

(17) Kingsbury, R. S.; Wang, J.; Coronell, O. Comparison of water and salt transport properties of ion exchange, reverse osmosis, and nanofiltration membranes for desalination and energy applications. *Journal of Membrane Science* **2020**, *604*, 117998.

(18) Ying, J.; Lin, Y.; Zhang, Y.; Jin, Y.; Li, X.; She, Q.; Matsuyama, H.; Yu, J. Mechanistic insights into the degradation of monovalent selective ion exchange membrane towards long-term application of real salt lake brines. *Journal of Membrane Science* **2022**, *652*, 120446.

(19) Virtanen, P. et al. SciPy 1.0: fundamental algorithms for scientific computing in Python. *Nature Methods* **2020**, *17*, 261–272.

(20) Liu, H.; She, Q. Influence of membrane structure-dependent water transport on conductivity-permselectivity trade-off and salt/water selectivity in electrodialysis: Implications for osmotic electrodialysis using porous ion exchange membranes. *Journal of Membrane Science* **2022**, *650*, 120398.

(21) Martí-Calatayud, M. C.; Buzzi, D. C.; García-Gabaldón, M.; Bernardes, A. M.; Tenório, J. A.; Pérez-Herranz, V. Ion transport through homogeneous and heterogeneous ion-exchange membranes in single salt and multicomponent electrolyte solutions. *Journal of Membrane Science* **2014**, *466*, 45–57.

(22) Długołecki, P.; Anet, B.; Metz, S. J.; Nijmeijer, K.; Wessling, M. Transport limitations in ion exchange membranes at low salt concentrations. *Journal of Membrane Science* **2010**, *346*, 163–171.

(23) Alkhadra, M. A.; Conforti, K. M.; Gao, T.; Tian, H.; Bazant, M. Z. Continuous Separation of Radionuclides from Contaminated Water by Shock Electrodialysis. *Environmental Science & Technology* **2019**, *54*, 527–536.

(24) Abu-Rjal, R.; Chinaryan, V.; Bazant, M. Z.; Rubinstein, I.; Zaltzman, B. Effect of concentration polarization on permselectivity. *Physical Review E* **2014**, *89*, 012302.

(25) Aydogan Gokturk, P.; Sujanani, R.; Qian, J.; Wang, Y.; Katz, L. E.; Freeman, B. D.; Crumlin, E. J. The Donnan potential revealed. *Nature Communications* **2022**, *13*, 1–7.

(26) Ahdab, Y. D.; Rehman, D.; Schücking, G.; Barbosa, M.; Lienhard, J. H. Treating Irrigation Water Using High-Performance Membranes for Monovalent Selective Electrodialysis. *ACS ES&T Water* **2021**, *1*, 117–124.

(27) Tedesco, M.; Hamelers, H. V.; Biesheuvel, P. M. Nernst-Planck transport theory for (reverse) electrodialysis: I. Effect of co-ion transport through the membranes. *Journal of Membrane Science* **2016**, *510*, 370–381.

(28) Ying, J.; Lin, Y.; Zhang, Y.; Yu, J. Developmental Progress of Electrodialysis Technologies and Membrane Materials for Extraction of Lithium from Salt Lake Brines. *ACS ES&T Water* **2023**, *3*, 1720–1739.

(29) Ding, D.; Yaroshchuk, A.; Bruening, M. L. Electrodialysis through nafion membranes coated with polyelectrolyte multilayers yields >99% pure monovalent ions at high recoveries. *Journal of Membrane Science* **2022**, *647*, 120294.

(30) Foo, Z. H.; Rehman, D.; Bouma, A. T.; Monsalvo, S.; Lienhard, J. H. Lithium Concentration from Salt-Lake Brine by Donnan-Enhanced Nanofiltration. *Environmental Science & Technology* **2023**, *57*, 6320–6330.

(31) Vera, M. L.; Torres, W. R.; Galli, C. I.; Chagnes, A.; Flexer, V. Environmental impact of direct lithium extraction from brines. *Nature Reviews Earth & Environment* **2023**, *4*, 149–165.

(32) Xu, P.; Hong, J.; Qian, X.; Xu, Z.; Xia, H.; Tao, X.; Xu, Z.; Ni, Q. Q. Materials for lithium recovery from salt lake brine. *Journal of Materials Science* **2021**, *56*, 16–63.

(33) Zhang, Y.; Hu, Y.; Wang, L.; Sun, W. Systematic review of lithium extraction from salt-lake brines via precipitation approaches. *Minerals Engineering* **2019**, *139*.

(34) Alkhadra, M. A.; Su, X.; Suss, M. E.; Tian, H.; Guyes, E. N.; Shocron, A. N.; Conforti, K. M.; Pedro De Souza, J.; Kim, N.; Tedesco, M.; Khoiruddin, K.; Wenten, G.; Santiago, J. G.; Hatton, T. A.; Bazant, M. Z. Electrochemical Methods for Water Purification, Ion Separations, and Energy Conversion. *Chemical Reviews* **2022**, *122*, 13547–13635.

(35) Palmer-Wilson, K.; Donald, J.; Robertson, B.; Lyseng, B.; Keller, V.; Fowler, M.; Wade, C.; Scholtysik, S.; Wild, P.; Rowe, A. Impact of land requirements on electricity system decarbonisation pathways. *Energy Policy* **2019**, *129*, 193–205.

(36) Mistry, K. H.; Lienhard, J. H. Generalized least energy of separation for desalination and other chemical separation processes. *Entropy* **2013**, *15*, 2046–2080.